AGU PUBLICATIONS

JGR

Journal of Geophysical Research: Space Physics

RESEARCH ARTICLE
10.1002/2017JA023931

Key Points:
- Compressional structures form at the Moon with deflections both parallel and antiparallel to upstream electric fields, but always outward
- Events with parallel and antiparallel velocity deflections have distinct characteristics and form under different solar wind conditions
- Momentum transfer between the solar wind and protons reflected from magnetic anomalies plays a key role in the formation of compressions

Correspondence to:
J. S. Halekas,
jasper-halekas@uiowa.edu

Citation:
Halekas, J. S., A. R. Poppe, C. Lue, W. M. Farrell, and J. P. McFadden (2017), Distribution and solar wind control of compressional solar wind-magnetic anomaly interactions observed at the Moon by ARTEMIS, *J. Geophys. Res. Space Physics*, *122*, doi:10.1002/2017JA023931.

Received 20 JAN 2017
Accepted 3 JUN 2017
Accepted article online 7 JUN 2017

Distribution and solar wind control of compressional solar wind-magnetic anomaly interactions observed at the Moon by ARTEMIS

J. S. Halekas[1,2], A. R. Poppe[2,3], C. Lue[1], W. M. Farrell[2,4], and J. P. McFadden[3]

[1]Department of Physics and Astronomy, University of Iowa, Iowa City, Iowa, USA, [2]Solar System Exploration Research Virtual Institute, NASA Ames Research Center, Moffett Field, California, USA, [3]Space Sciences Laboratory, University of California, Berkeley, California, USA, [4]NASA Goddard Space Flight Center, Greenbelt, Maryland, USA

Abstract A statistical investigation of 5 years of observations from the two-probe Acceleration, Reconnection, Turbulence, and Electrodynamics of Moon's Interaction with the Sun (ARTEMIS) mission reveals that strong compressional interactions occur infrequently at high altitudes near the ecliptic but can form in a wide range of solar wind conditions and can occur up to two lunar radii downstream from the lunar limb. The compressional events, some of which may represent small-scale collisionless shocks ("limb shocks"), occur in both steady and variable interplanetary magnetic field (IMF) conditions, with those forming in steady IMF well organized by the location of lunar remanent crustal magnetization. The events observed by ARTEMIS have similarities to ion foreshock phenomena, and those observed in variable IMF conditions may result from either local lunar interactions or distant terrestrial foreshock interactions. Observed velocity deflections associated with compressional events are always outward from the lunar wake, regardless of location and solar wind conditions. However, events for which the observed velocity deflection is parallel to the upstream motional electric field form in distinctly different solar wind conditions and locations than events with antiparallel deflections. Consideration of the momentum transfer between incoming and reflected solar wind populations helps explain the observed characteristics of the different groups of events.

Plain Language Summary We survey the environment around the Moon to determine when and where strong amplifications in the charged particle density and magnetic field strength occur. These structures may be some of the smallest shock waves in the solar system, and learning about their formation informs us about the interaction of charged particles with small-scale magnetic fields throughout the solar system and beyond. We find that these compressions occur in an extended region downstream from the lunar dawn and dusk regions and that they can form under a wide variety of solar wind conditions. However, we find that two distinctly different types of interactions occur for different magnetic field geometries and solar wind conditions. The two types of events appear to differ because of the different trajectories followed by solar wind protons that reflect from localized lunar magnetic fields and the resulting differences in how the incoming solar wind from upstream interacts with these reflected particles.

1. Introduction

Magnetometer measurements on the lunar surface [*Dyal et al.*, 1970] and from orbit [*Coleman et al.*, 1972a, 1972b] in the Apollo era first revealed the existence of remanent crustal magnetization on the Moon. Subsequent mapping of remanent fields has shown that they have small coherence scales, with orbital measurements [*Hood et al.*, 2001; *Mitchell et al.*, 2008; *Tsunakawa et al.*, 2015] indicating spatial structure down to the altitude-limited resolution of tens of kilometers, and surface measurements [*Dyal et al.*, 1974] revealing significant variability in magnitude and polarity even at subkilometer scales. At the surface, lunar fields can reach several hundred nanotesla or more, but their incoherence ensures that the fields decrease to at most a few tens of nanotesla within ~30 km from the surface, with even those strengths achieved above only a few localized regions of the surface. Therefore, lunar magnetic fields present a highly incoherent obstacle to the solar wind, with their direct influence only appreciable within a small fraction of an ion inertial length from the surface, seemingly too localized to produce a coherent disturbance in the solar wind [*Omidi et al.*, 2002].

Despite their diminutive scale, the presence of lunar magnetic anomalies results in observable macroscopic perturbations to the solar wind, in the form of compressional disturbances that extend downstream from

near the lunar limb, variously termed "limb perturbations," "limb shocks," "limb compressions," and "lunar external magnetic enhancements" [*Ness et al.*, 1968; *Whang and Ness*, 1970; *Colburn et al.*, 1971; *Sonett and Mihalov*, 1972; *Schubert and Lichtenstein*, 1974; *Russell and Lichtenstein*, 1975; *Lin et al.*, 1998; *Halekas et al.*, 2006, 2008, 2014; *Nishino et al.*, 2012]. Though the earliest observations of these features occurred before those of the magnetic sources whose presence apparently leads to their formation, all subsequent studies have confirmed a causal link with lunar remanent magnetism. The exact nature of the disturbances remains uncertain, and indeed, they may well span a range of different modes of interaction, but recent work has shown that at least some cases have many observational characteristics consistent with small-scale collisionless shocks [*Halekas et al.*, 2014].

Until recently, the formation mechanism(s) remained elusive, given the apparent difficulty of such small-scale sources producing macroscopic perturbations in the solar wind. Indeed, global simulations could only reproduce observations with stronger than observed magnetic fields and/or complex multipolar geometries [*Harnett and Winglee*, 2000, 2003]. However, significant local reflection of solar wind protons by magnetic anomalies, observed by Nozomi [*Futaana et al.*, 2003] and confirmed by Kaguya [*Saito et al.*, 2010] and Chandrayaan-1 [*Wieser et al.*, 2010; *Lue et al.*, 2011], provides a potential formation mechanism. Observations [*Saito et al.*, 2012; *Futaana et al.*, 2013] and hybrid and particle-in-cell simulations [*Deca et al.*, 2014, 2015; *Jarvinen et al.*, 2014; *Giacalone and Hood*, 2015] suggest that protons reflect in large part from polarization and/or Hall electric fields driven by the coupling between incoming protons and electrons reflected from the localized magnetic field gradient. Regardless of the mechanism, the observed reflection can reach levels of up to 50%, producing a plume of reflected protons with significant density and a high relative velocity with respect to the incoming solar wind, which spreads out as the reflected protons gyrate downstream. This plume of reflected protons effectively multiplies the scale of the region with which the incoming solar wind can interact.

Fatemi et al. [2014] performed the first global hybrid simulations of the solar wind-magnetic anomaly interaction that took into account the presence of reflected protons. They found that the introduction of a reflected population of protons led to the formation of compressional disturbances similar to those observed by orbiting spacecraft. The *Fatemi et al.* [2014] simulations lack a self-consistent description of the reflection process but still reproduce observations, suggesting that the physics of the high-altitude macroscale interactions can to some degree be decoupled from the low-altitude microphysics of the solar wind proton reflection that drives them.

In the *Fatemi et al.* [2014] simulation, the strongest compressional disturbances occurred near the flank of the Moon where the solar wind motional electric field pointed toward the surface. Intriguingly, both limb shock events analyzed by *Halekas et al.* [2014] shared this geometry. These results could support an interpretation in which momentum transfer between reflected and incoming solar wind protons plays a role in the formation of limb compressional disturbances, since for this geometry the motional electric field acts to decelerate reflected protons as they travel outward from the Moon, which (assuming other forces remain constant) causes a corresponding outward deflection of the solar wind in order to conserve linear momentum. Figure 1 shows a schematic illustration of this geometry and the respective forces on the reflected and solar wind ion populations. A key question is whether the formation of compressional disturbances requires this geometry or whether compressional events can also occur for other interplanetary magnetic field (IMF) geometries.

In this manuscript, we survey compressional disturbances observed by the two-probe Acceleration, Reconnection, Turbulence, and Electrodynamics of Moon's Interaction with the Sun (ARTEMIS) mission outside of the lunar wake in order to determine when and where they occur and what solar wind and IMF conditions favor their occurrence.

2. Compressional Solar Wind-Magnetic Anomaly Interactions Observed by ARTEMIS

The two-probe ARTEMIS mission [*Angelopoulos*, 2011] provides a unique capability to distinguish Moon-related disturbances from solar wind transients. We first discuss three Moon-related compressional events observed by ARTEMIS in order to introduce the observations and define different types of events.

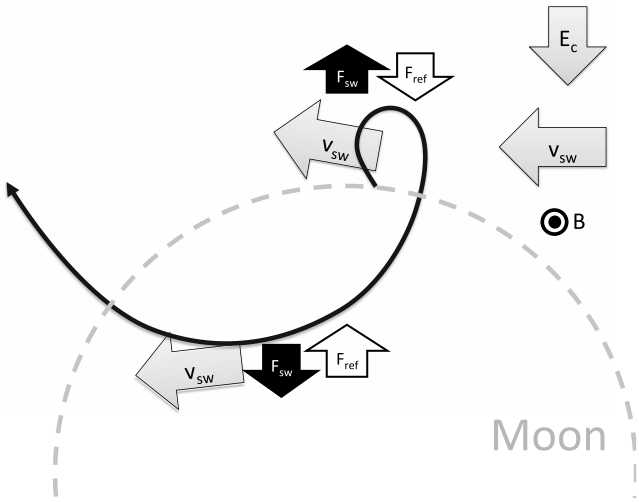

Figure 1. Schematic illustration of the geometry of compressional solar wind-magnetic anomaly interactions simulated by *Fatemi et al.* [2014] and observed by *Halekas et al.* [2014]. For these events, the upstream motional electric field of the solar wind (E_c) pointed toward the lunar surface near the limb. Reflected protons would therefore be initially decelerated by the force associated with this electric field (F_{ref}), in turn resulting in a corresponding outward force (F_{sw}) on the solar wind, in order to conserve linear momentum. At later points in the reflected proton's trajectories, after they have accelerated to velocities higher than the solar wind (if they have not impacted the Moon), the forces between the two ion populations would switch direction as shown (see section 5 for discussion and detailed force equations).

Figures 2 and 3 show two events fortuitously observed on successive days in nearly the same location during periods of steady IMF, but with roughly oppositely directed IMF and therefore oppositely directed upstream motional electric field. For both of these events, we observe deflections of the solar wind outward from the Moon (in the $-y$ direction given the location of the near-Moon probe on the $-y$ side of the Moon at this time). For the event in Figure 3 (an "antiparallel" case), the observed velocity deflection is approximately antiparallel to the upstream electric field, consistent with the geometry shown in Figure 1. For the event in Figure 2 (a "parallel" case), the observed deflection is approximately parallel to the upstream electric field, seemingly inconsistent with the geometry shown in Figure 1 if the solar wind deflection occurs near the reflection point.

The two events have many similar characteristics, including low solar wind proton temperatures and very steady upstream IMF and flow velocity, compression factors of 1.5–2.0 in both magnetic field and density, outward velocity deflections of ~60–80 km/s, visible signs of electron heating in the electron energy spectra, and visible changes in the energy spectra of both solar wind protons and alphas. Note that changes in spacecraft potential that shift the electron energy range at ~16:54:30 in Figure 2 and ~17:47:40 in Figure 3 result from changes in the biasing of the electric field probes routinely performed prior to shadow entry. Discontinuities in electron temperature at these bias changes cannot be considered reliable; however, the subsequent changes in temperature appear robust.

However, the events in Figures 2 and 3 also have clear observational differences. The event of Figure 2 has a very strong IMF, implying a low Alfvén Mach number M_A, ion β, and convected ion gyroradius r_c. Also, while both events have clear non-solar wind ion populations, the non-solar wind ions in the parallel case of Figure 2 appear at energies above the solar wind, while those in the antiparallel case of Figure 3 appear at energies below the solar wind. Commensurate with this difference, the flow-aligned ($-x$ component) velocity displays a more significant change in the antiparallel case, with a ~40 km/s slowdown contiguous with the low-energy ion population preceding the main transverse deflection (large $-\Delta v_y$ at ~17:50:30). These low-energy ions appear consistent with a locally reflected population in a foot region [*Bale et al.*, 2005], with their addition causing the change in the flow-aligned bulk velocity moment, while the transverse velocity deflection instead represents a change in the velocity of the solar wind core, as observed by *Halekas et al.* [2014]. In contrast, the parallel case has a smaller ~20 km/s slowdown contiguous with the main transverse deflection (large $-\Delta v_y$ at ~16:56:30), not associated with the additional ion population at higher energies, but instead representing a change in the velocity of the core population.

We observe a somewhat different interaction associated with rotations in the IMF, as shown in one example in Figure 4. For this event we find no clear indication of a non-solar wind ion population, but we do still observe compression in both density and magnetic field, and an outward velocity deflection of ~60 km/s. When accounting for solar wind propagation time from the upstream probe, the compressional feature observed by the near-Moon probe occurs coincident with a significant rotation in the IMF. Other events identified during variable IMF conditions share similar characteristics.

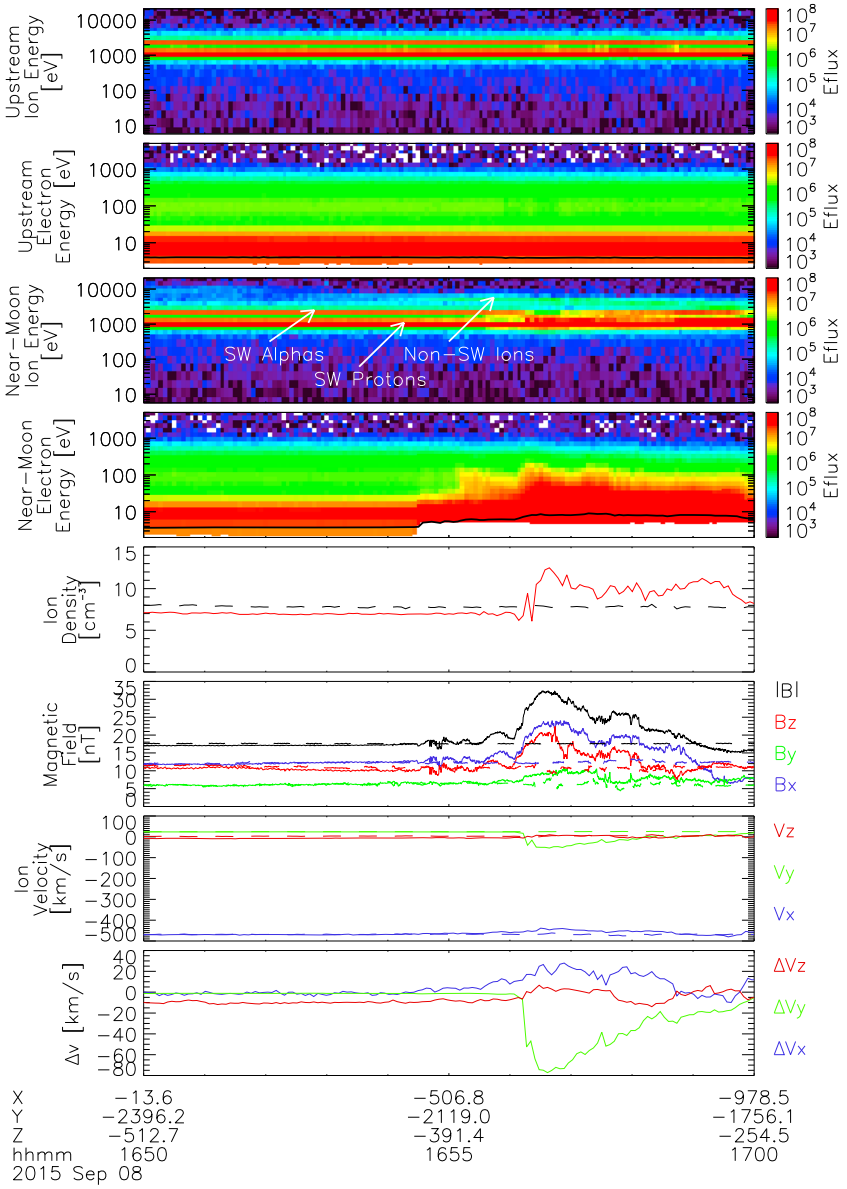

Figure 2. Event with upstream motional electric field roughly parallel to the observed velocity deflection, with panels showing upstream ion and electron energy spectra (corrected for spacecraft potential) in units of eV/[cm^2 s sr eV]; near-Moon ion and electron energy spectra (corrected for spacecraft potential) in the same units; upstream (dashed) and near-Moon (solid) ion density, magnetic field, and velocity; and the velocity deflection calculated by differencing the near-Moon from the upstream velocity. The black lines on electron energy spectra show scalar electron temperature. All vector quantities utilize SSE coordinates. Text labels indicate the position of the near-Moon probe.

Although only one of the two ARTEMIS probes observed the compressional feature, suggesting a lunar interaction, we cannot completely discount the possibility that the event in Figure 4 represents a terrestrial foreshock interaction. Hot flow anomalies (HFAs) commonly occur when a tangential IMF discontinuity comes into contact with the Earth's bow shock with an orientation that favors the channeling of reflected ions along the discontinuity [*Schwartz*, 1995; *Thomas et al.*, 1991; *Omidi and Sibeck*, 2007]. Given the significant ARTEMIS probe separation of ~16,000 km at this time, it appears within the realm of possibility that only one probe could observe an HFA, even given their large scale size (many Earth radii), especially if the presence of the Moon locally altered the interaction and shielded one probe from the HFA's effects. The position of the Moon at this time (GSE coordinates of ~[5, −60, 0] Earth radii) could conceivably place it in the ion foreshock, given the $+B_y$ field observed before the discontinuity and the $+B_x/+B_y$ field after its passage. However, though

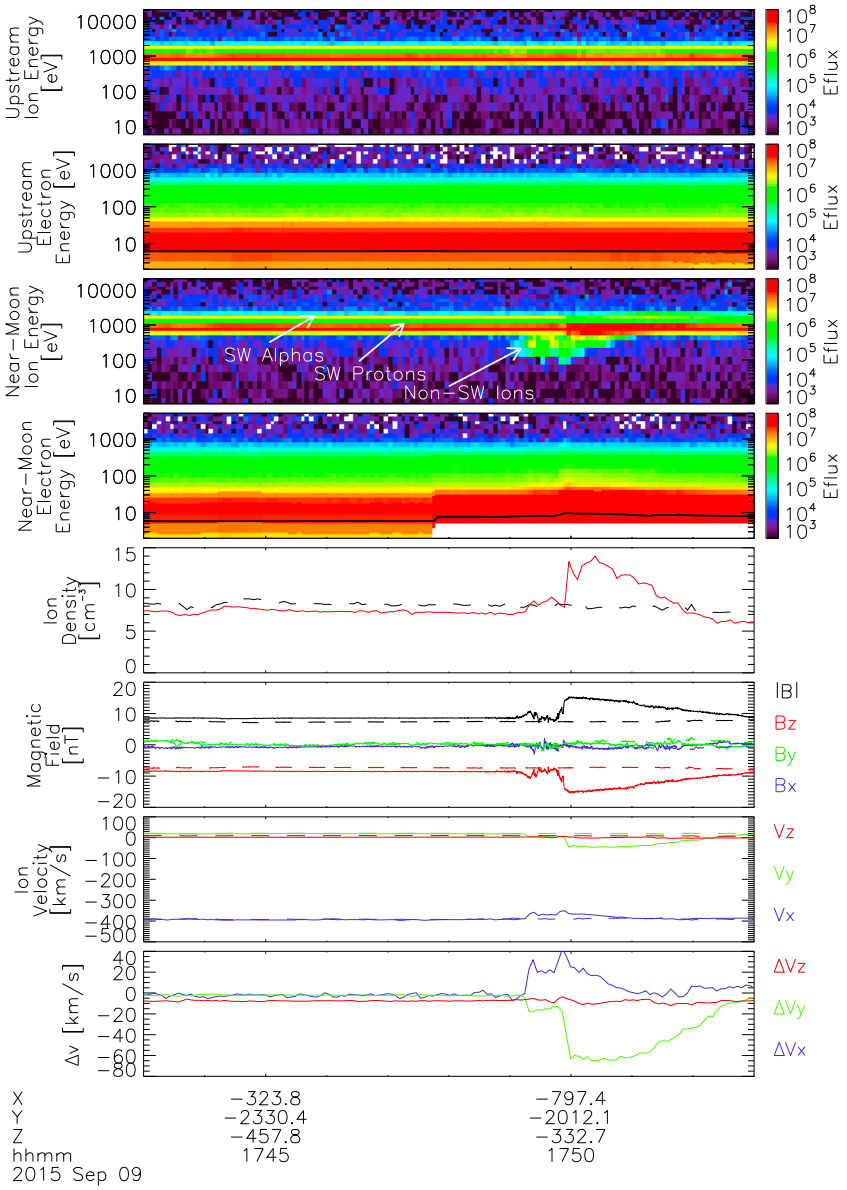

Figure 3. Event with upstream motional electric field roughly antiparallel to the observed velocity deflection, with all panels and labels the same as Figure 2.

ARTEMIS observed some atypical electron signatures shortly before the event, it did not observe any of the high-energy reflected proton populations typically seen in the ion foreshock at lunar distances. Furthermore, it appears challenging to explain why terrestrial foreshock phenomena would produce events organized in lunar coordinates, and also why they would always lead to a velocity deflection outward from the lunar wake.

As an alternative, we propose the possibility of a localized HFA-like interaction, wherein reflected protons from the Moon interact with a solar wind discontinuity on a much smaller scale than a terrestrial HFA. Only a detailed analysis of a larger sample of such events (beyond the scope of this paper) could definitively answer whether these events represent localized lunar interactions, terrestrial foreshock events, or perhaps some mix of the two. Either would represent an interesting conclusion. A lunar interaction would represent perhaps the smallest HFA-like interaction ever observed, while a terrestrial foreshock event would represent a very distant observation of such a phenomenon.

A third type of compressional interaction also occurs occasionally. As shown by previous authors, including *Nakagawa et al.* [2012] and *Halekas et al.* [2013], large-amplitude ultralow-frequency (ULF) waves can occur

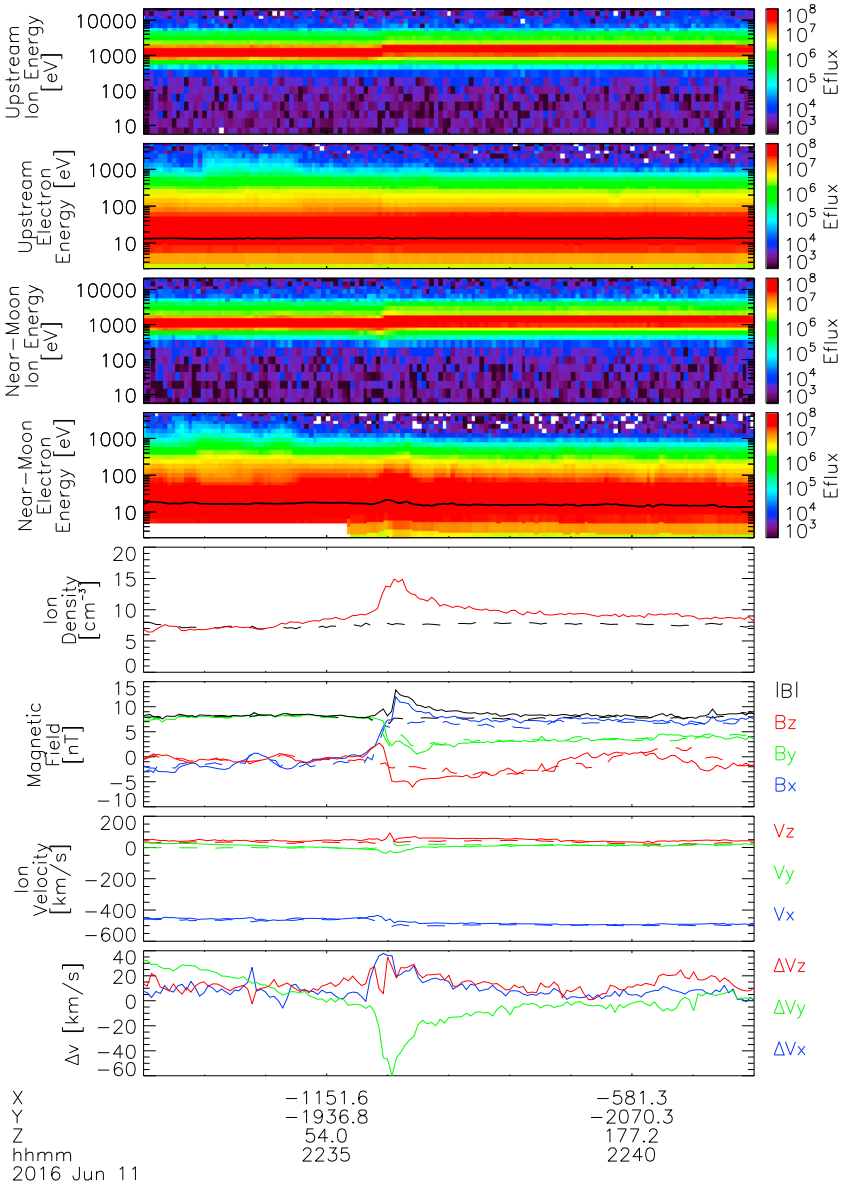

Figure 4. Event observed during variable IMF conditions, with all panels and labels the same as Figures 2 and 3. In this case, we time-shifted the upstream observations by 40 s to account for propagation delays between the two probes.

near the Moon, presumably driven by resonant interactions between the solar wind and reflected protons. These ULF waves can steepen and become compressive, but they typically do not produce compressions as large or as coherent as those shown in Figures 2–4, or velocity deflections as significant as for those events. Sometimes, ULF waves occur as precursors to the coherent events discussed above. Since others have discussed these waves previously, we do not show an example of this type of event in this manuscript.

3. Statistical Distribution of Compressional Interactions

We utilized the directly comparable measurements from the two probes to conduct an automated search for all compressional disturbances caused by the presence of the Moon, with selection criteria designed to find events similar to those discussed in the previous section. We considered all observations made between 1 September 2011 and 31 July 2016 when both probes were outside of a cone extending downstream from the lunar limb with a 6° opening angle, the lunar phase was within a 110° (~8.9 days) range before or after new Moon, and the measured flow velocity was greater than 250 km/s. These three criteria, though

Table 1. Compressional Solar Wind-Magnetic Anomaly Interaction Events Observed by ARTEMIS, Sorted by Event Type and by the Alignment of the Upstream Motional Electric Field, and the Observed Velocity Deflection (for Each Event, $\left\langle \hat{E}\cdot\widehat{\Delta v}\right\rangle$ Represents the Mean Dot Product Between Unit Vectors in the Direction of the Upstream Motional Electric Field and the Observed Velocity Deflection Associated With the Compressional Event, Averaged Over the Entire Event)

Type of Event	$\left\langle \hat{E}\cdot\widehat{\Delta v}\right\rangle < -0.5$	$-0.5 < \left\langle \hat{E}\cdot\widehat{\Delta v}\right\rangle < 0.5$	$-0.5 < \left\langle \hat{E}\cdot\widehat{\Delta v}\right\rangle$	Total
Steady	9	4	7	20
Variable	3	9	0	12
ULF	2	3	1	6
Total	14	16	8	38

arguably overly conservative, and neglecting asymmetries due to velocity aberration, successfully excluded all times when either probe crossed the lunar wake or entered the terrestrial magnetosphere, without the need for labor-intensive manual event selection. Within the selected time ranges, we identified all intervals for which both the magnetic field magnitude measured by fluxgate magnetometer (FGM) [*Auster et al.*, 2008] and the total plasma density from onboard ion density moments derived from Electrostatic Analyzer (ESA) data [*McFadden et al.*, 2008] increased by 50% or more at the near-Moon probe as compared to the corresponding measurements by the more distant upstream probe. This threshold is more conservative than previous studies [*Sonett and Mihalov*, 1972; *Whang and Ness*, 1970] but has the advantage of resulting in dramatically fewer false positive events. After manually removing a small number of false positives caused by bad data points and mode switches, we arrived at a final list of 38 events, for which we saved each individual measurement taken during the full extent of the disturbance (including portions surrounding the peak with less than a 50% amplification). Both events from *Halekas et al.* [2014] qualify for this event list.

We classified our 38 events by event type ("steady," "variable," or "ULF") and geometry (determined by the dot product between unit vectors in the direction of the upstream motional electric field and the observed velocity deflection), as tabulated in Table 1. Coherent compressional events occurred during both steady (e.g., Figures 2 and 3) and variable (e.g., Figure 4) IMF conditions. We defined an event as occurring in variable IMF conditions if there was an IMF rotation of $\gtrsim$30° observed by the upstream probe within the duration of the compressional amplification observed by the near-Moon probe. In addition, several events occurred as a steepened portion of an ultralow-frequency (ULF) wave train. The few events that we placed into this category were marginal, in the sense that they only satisfied the 50% field magnitude and density amplification criteria for a very brief time period, typically a small fraction of the observed ULF wave train. We classified coherent compressional events that included ULF precursor activity as steady or variable events as appropriate but noted the presence of precursors. Identified events also occurred for a variety of geometries, with the observed solar wind velocity deflections sometimes close to antiparallel to the upstream motional electric field (as shown schematically in Figure 1 and valid for the event shown in Figure 3 as well as the simulation of *Fatemi et al.* [2014] and the two events observed by *Halekas et al.* [2014]) but in other cases close to perpendicular or close to parallel to the upstream electric field (for example, the event shown in Figure 2).

Figures 5 and 6 show the distribution of the events in Table 1 in Selenocentric Solar Ecliptic (SSE) coordinates, for each measurement in Figure 5 and for the point with maximum velocity deflection for each event in Figure 6. The events observed by ARTEMIS occur in a wedge near the equatorial plane, beginning near the limb and extending downstream roughly two lunar radii, and covering angles from ~7° to 40° from the Moon-Sun line (x axis) with respect to the limb. The clear organization of events around the Moon confirms the effectiveness of our selection criteria. The clustering near the equatorial plane results from sampling bias due to the near-equatorial orbits of the two ARTEMIS probes. The ARTEMIS probe orbits have aposelenes of ~10–12 lunar radii (~17,000–20,000 km), so the sampling within the equatorial plane should more accurately represent the true distribution of events. The distribution observed by ARTEMIS agrees in most respects with that observed by Explorer 35 [*Whang and Ness*, 1970; *Sonett and Mihalov*, 1972], though those previous studies used only magnetic field data to identify events.

ARTEMIS observes almost entirely outward (with respect to the Moon and its wake) velocity deflections, regardless of the orientation of the IMF and upstream motional electric field. The largest deflections (on the order of 10°) could potentially have been detected by Explorer 35, which reported only tentative detections of outward deflections on the order of ~3° [*Siscoe et al.*, 1969]. However, given the low probability of

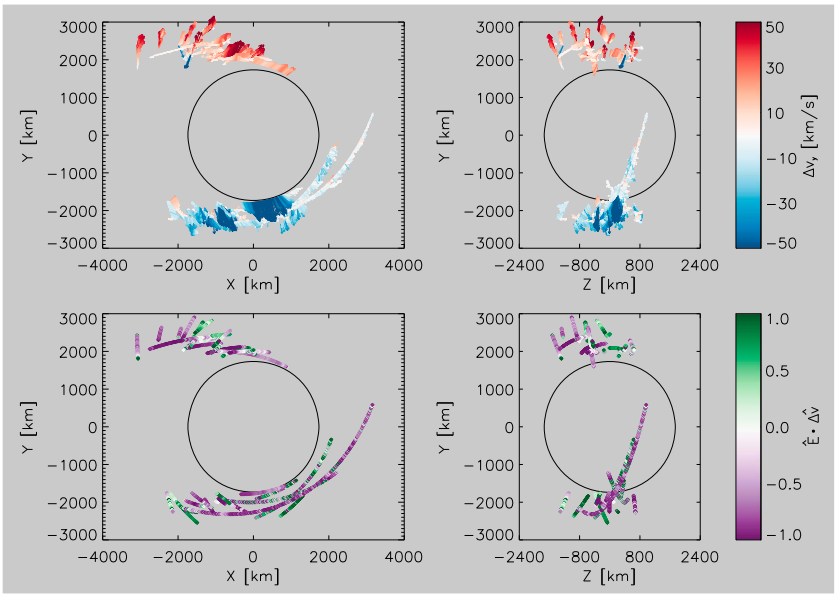

Figure 5. The top two panels show observed vector velocity deflections during all identified events, in Selenocentric Solar Ecliptic (SSE) coordinates, colored by Δv_y (red = positive, blue = negative). The bottom two panels show the degree of alignment of the observed velocity deflection with the upstream motional electric field E (green = parallel, purple = anti parallel).

occurrence, the overall average deflection outside the wake remains vanishingly small even with modern instrumentation, and indeed, mission-averaged velocity fields show no hint of these few events [*Zhang et al.*, 2014].

Though compressional events occur under all IMF geometries, several distinct trends appear for different types of events and geometries. Events with velocity deflections parallel to the upstream motional electric field (green points in the bottom rows of Figures 5 and 6) tend to occur closer to the equator ($z = 0$) and at a higher angle from the Moon-Sun line (x axis) with respect to the limb than those with velocity deflections antiparallel to the upstream electric field (purple points in the bottom rows of Figures 5 and 6). Events occurring during variable IMF conditions (diamonds) occur closer to the limb and extend less far downstream. Events consisting of steepened ULF waves (pluses) occur exclusively on the dawnside and extend farther upstream than other types of events, consistent with direct IMF connection to the surface under nominal Parker spiral IMF geometry.

While we cannot uniquely determine the exact source of the events observed by ARTEMIS, we can estimate what regions of the lunar surface might have caused them. Based on previous results [*Whang and Ness*, 1970; *Sonett and Mihalov*, 1972; *Schubert and Lichtenstein*, 1974; *Russell and Lichtenstein*, 1975; *Halekas et al.*, 2014], which have shown that magnetic sources near and just upstream from the lunar limb are responsible for producing the majority of compressions, we assume that a region 30° sunward of the terminator plays a dominant role in generating compressions near and downstream from the limb. Figure 7 shows inferred source regions under this assumption, demonstrating that the majority of the events observed during steady IMF conditions have sources that cluster in the strong southern farside magnetic anomalies, in agreement with previous results. Events observed during variable IMF conditions, on the other hand, have sources in a band around the equator, displaying no obvious correlation with crustal magnetic fields.

4. Solar Wind Control of Compressional Interactions

We next investigated whether compressional disturbances form near the Moon more frequently for specific solar wind conditions. Explorer 35 observations suggested that strong compressional disturbances occur more frequently under high plasma β conditions [*Whang and Ness*, 1972], while Lunar Prospector identified more events near the limb for higher solar wind proton density, lower proton temperature, lower thermal

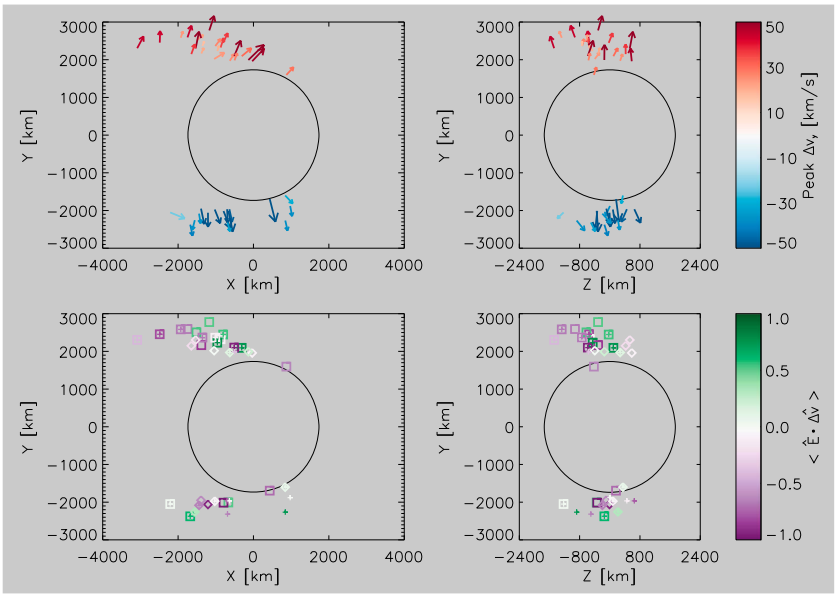

Figure 6. (top row) The vector velocity deflections for each identified event, with the vector length corresponding to the magnitude of the peak velocity deflection. (bottom row) The average degree of alignment of the observed velocity deflection with the upstream motional electric field *E*, with a point for each event located at the time of maximum velocity deflection. In Figure 6 (bottom row), the squares represent steady IMF events, the diamonds represent variable IMF events, and the plus signs indicate steepened ULF waves (corresponding to the categories of Table 1). The plus signs inside of squares or diamonds indicate ULF precursors for coherent events.

proton gyroradius, and lower β_p (in conflict with the preceding study) [*Halekas et al.*, 2006]. In this work, we consider a wider array of solar wind parameters, accessible to us thanks to the comprehensive measurements from the ARTEMIS FGM and ESA instruments.

Figure 8 shows a sample of the parameters we considered. Compared to the overall distribution of measurements for the same range of lunar phases (gray-scale frequency distributions), we find that strong compressional disturbances (colored points) occur more frequently at the ARTEMIS orbit for conditions with low proton temperature, low ion inertial length, and low convected ion gyroradius, and in the away (cone angle $>$90°) IMF sector. Most of these trends agree with previous work. We suggest that the increased probability for events to occur in the away sector could relate to ARTEMIS's equatorial orbit and the dominant effects of

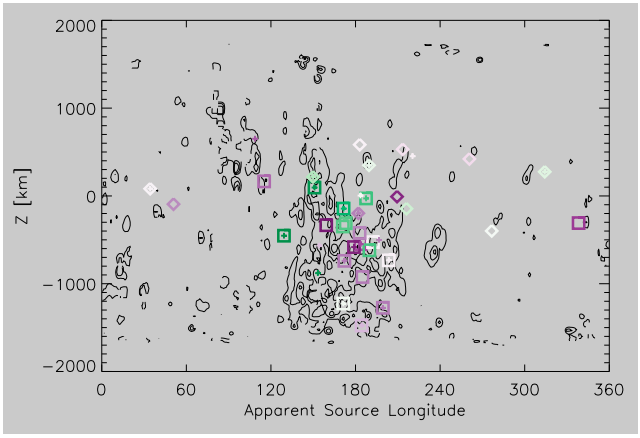

Figure 7. Surface locations 30° in longitude sunward of the terminator and at the same SSE *z* coordinate as events observed by ARTEMIS, along with 20, 50, and 100 nT contours of surface magnetic field estimated from Lunar Prospector Electron Reflectometer measurements [*Mitchell et al.*, 2008]. Event symbols and color code are the same as in Figure 6.

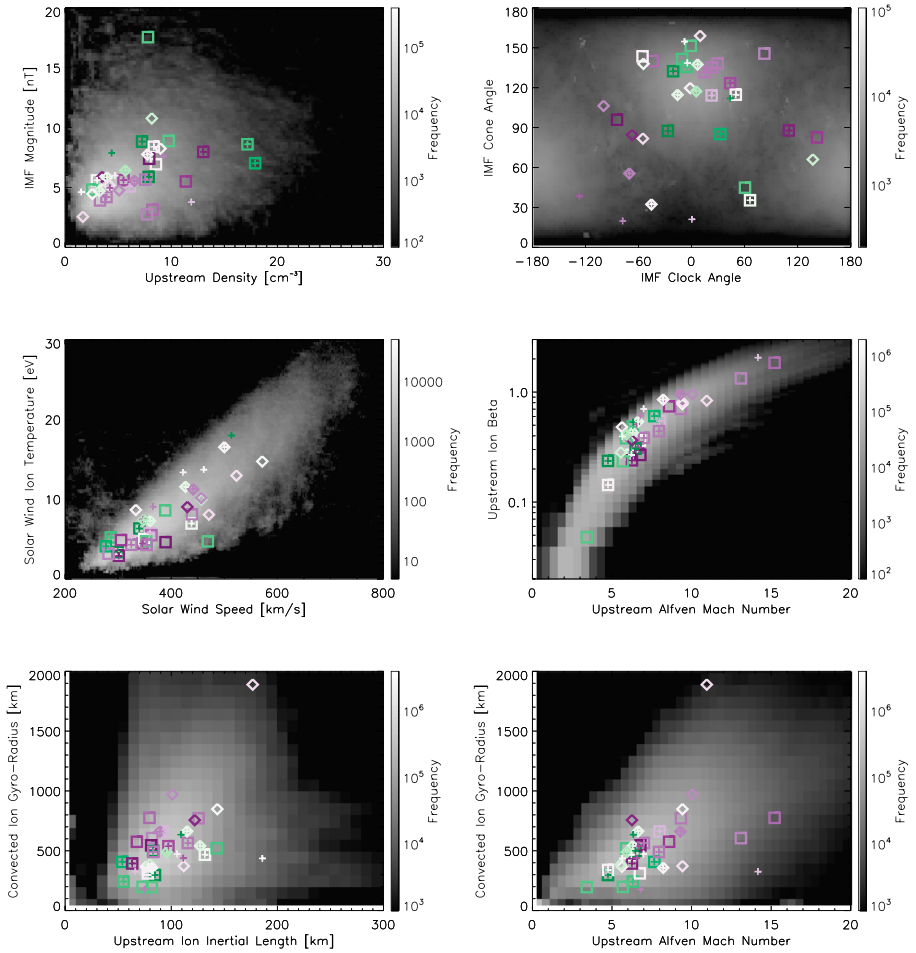

Figure 8. Distribution of upstream solar wind parameters during compressional events observed by ARTEMIS (same symbols and color code as Figures 6 and 7) compared to the overall statistical distribution of solar wind parameters observed by ARTEMIS over its entire mission, for the same range of lunar phases (gray-scale 2-D frequency distributions). We define cone angle as the angle between the IMF and the SSE *x* axis and clock angle as the angle from the *y* axis in the *y-z* plane, with positive angles representing positive *z*. We define the Alfvén Mach number $M_A = v_{sw}/\left(\frac{B}{\sqrt{\mu_o m_p n_p}}\right)$, $\beta_p = n_p k T_p/\left(\frac{B^2}{2\mu_o}\right)$, ion inertial length $D_p = c/\omega_{pi}$, and convected ion gyroradius $r_c = \frac{mv_{sw\perp}}{qB}$.

the southern farside anomalies, since in the away sector reflected protons from these anomalies will gyrate northward, more plausibly affecting the region near the equator.

Intriguingly, we find a clear dichotomy between events with velocity deflections parallel to the upstream motional electric field (green points) and those with antiparallel deflections (purple points), with the two groups of events occurring under distinctly different solar wind conditions. Antiparallel cases (like those from *Fatemi et al.* [2014] and *Halekas et al.* [2014]) occur more often at times with lower magnetic field, IMF more out of the ecliptic, higher solar wind speed, higher M_A and β_p, and higher r_c, in comparison to parallel cases. Interestingly, these trends appear to hold across all event types, including variable IMF and ULF cases, suggesting that common processes may in fact lead to the formation of the different types of events. We also note that the difference in favored Mach numbers helps explain the spatial grouping of events found in Figures 5 and 6, with low M_A events (most parallel cases) more likely to extend farther laterally from the limb, and high M_A events (most antiparallel cases) confined closer to the wake boundary.

5. Macroscopic Forces on the Solar Wind

In the penultimate section of this paper, we consider the macroscopic forces responsible for slowing and/or deflecting the solar wind. Ultimately, these forces must lead to the formation of a compression and/or shock

near the Moon. Following *Chapman and Dunlop* [1986] and *Sauer et al.* [1994] we write the macroscopic force on the solar wind and reflected protons in a two fluid approximation, assuming isotropic plasma pressure:

$$\boldsymbol{F}_{sw} = m_p n_{sw}\left(\frac{\partial}{\partial t} + \boldsymbol{v}_{sw}\cdot\nabla\right)\boldsymbol{v}_{sw} = \frac{n_{sw}}{n_e}\left[q n_{ref}(\boldsymbol{v}_{sw} - \boldsymbol{v}_{ref})\times\boldsymbol{B} + \boldsymbol{J}\times\boldsymbol{B} - \nabla P_e\right] - \nabla P_{sw} \quad (1)$$

$$\boldsymbol{F}_{ref} = m_p n_{ref}\left(\frac{\partial}{\partial t} + \boldsymbol{v}_{ref}\cdot\nabla\right)\boldsymbol{v}_{ref} = \frac{n_{ref}}{n_e}\left[q n_{sw}(\boldsymbol{v}_{ref} - \boldsymbol{v}_{sw})\times\boldsymbol{B} + \boldsymbol{J}\times\boldsymbol{B} - \nabla P_e\right] - \nabla P_{ref} \quad (2)$$

Equations (1) and (2) incorporate the usual fluid pressure gradient and $J \times B$ forces, with the latter separable into magnetic pressure and curvature/tension terms in the standard fashion, but also include the momentum transfer between the solar wind and reflected protons. This set of coupled equations assumes quasi-neutrality ($n_e = n_{sw} + n_{ref}$) and therefore neglects direct consideration of polarization electric fields. Note that adding the two equations together allows one to recover the usual one-fluid MHD momentum equation.

In the limit of low initial reflected velocity, equations (1) and (2) describe ion pickup and mass loading, with the reflected (pickup) species initially accelerating in the direction of the upstream motional electric field, and the solar wind deflecting in the opposite direction to conserve momentum. Similar considerations hold for reflected protons, particularly in antiparallel cases where the reflected protons initially decelerate and thus have relatively low velocities (as shown in the schematic example of Figure 1). On the other hand, at later points in their trajectories where reflected (or pickup) proton velocities exceed the solar wind speed, the sign of the coupling force term changes, the reflected (or pickup) population gyrates in the opposite direction from the upstream motional electric field, and the solar wind deflects back in the direction of the upstream motional electric field (also shown in Figure 1). Over large distance scales this momentum interchange continues in a cyclical fashion, leading to a periodic rotation of the two populations in velocity space around their common center of mass velocity.

Omidi and Sibeck [2007] have discussed the formation of shocks under different motional electric fields, describing a "solitary shock" that forms in cases where the upstream motional electric field points toward the shock. Solitary shocks, closely analogous to our antiparallel events, have a more spatially confined structure that forms farther upstream from the obstacle, with a more turbulent downstream region, in comparison to quasi-perpendicular shocks with the opposite geometry. The solitary shock profiles shown by Omidi and Sibeck have several similarities to the antiparallel event of Figure 3, including a slowdown preceding the transverse velocity deflection. Omidi and Sibeck discussed these structures in terms of fast mode wave propagation, but we can also consider the force balance and momentum transfer in a multifluid picture. In the solitary shock case, reflected protons gyrate upstream, and the solar wind experiences a momentum coupling force that reinforces pressure gradient and $J \times B$ forces, while in the opposite geometry reflected protons gyrate downstream, and the coupling forces oppose the fluid forces near the reflection point.

With these considerations in mind, we plot the observed velocity deflection versus compression ratios related to each of the main terms of the force exerted on the solar wind fluid (equation (1)) in Figures 9 and 10, in an attempt to determine their relative importance. In general, observed velocity deflections do not correlate well with either the near-Moon to upstream density ratio or ion pressure ratio (linear and rank correlation coefficients near zero), regardless of event geometry. On the other hand, observed velocity deflections do correlate better with the near-Moon to upstream magnetic field and electron pressure ratios (linear correlation coefficients of 0.13 and 0.37, respectively, and rank correlation coefficients of 0.37 and 0.53, with less than a 2% and 0.07% chance, respectively, of these rank correlations arising by chance). The correlations are even better for cases with antiparallel deflections (linear correlation coefficients of 0.68 and 0.80, respectively). These strong correlations suggest that both magnetic pressure and electron pressure play a significant role in deflecting the solar wind (consistent with the observation that these events have an average β on the order of unity). Intriguingly, both of these terms ultimately relate to the electron dynamics (the magnetic field increase at a shock arises self-consistently as a result of electron drifts across the shock surface). The larger magnetic field ratios observed for antiparallel cases, which Figure 8 shows predominantly occur for higher β conditions, appear to support the conclusions of *Whang and Ness* [1972].

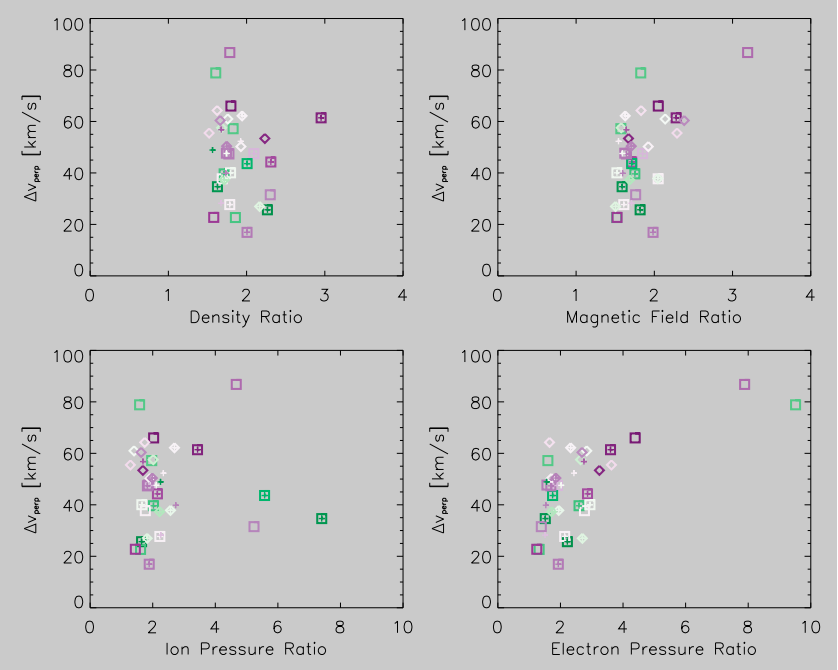

Figure 9. Peak transverse velocity deflection versus near-Moon to upstream ratios of plasma density, magnetic field magnitude, and ion and electron thermal pressure (same symbols and color code as Figures 6–8).

The pressure gradient and magnetic pressure/tension forces should arise self-consistently across a compressional discontinuity or shock. On the other hand, the momentum coupling force exists regardless of whether compression occurs. Dimensional analysis of equation (1) suggests that the relative importance of the momentum transfer term should scale as $\sim n_{ref}\, v\, B/(B^2/L) = n_{ref}\, v\, L/B$, proportional to the product of the reflected proton density, the convected ion gyroradius r_c, and the discontinuity gradient length scale L. Assuming a transition scale on the order of the convected ion gyroradius on the downstream side $r_{c,d}$ [*Bale et al.*, 2003], the relative weight of the momentum coupling force should then scale very roughly as $\sim n_{ref}\, r_c^2$. Figure 10 shows that consistent with these expectations, events with larger r_c have larger velocity deflections for antiparallel cases (for which all the force terms on the solar wind should reinforce near the reflection point). On the other hand, for parallel cases, the velocity deflections show the opposite trend, with the highest deflections observed for low r_c. We speculate that for events with low r_c, the smaller scale of the trajectory leads to higher local reflected proton densities, allowing the momentum coupling force to still reach significant levels.

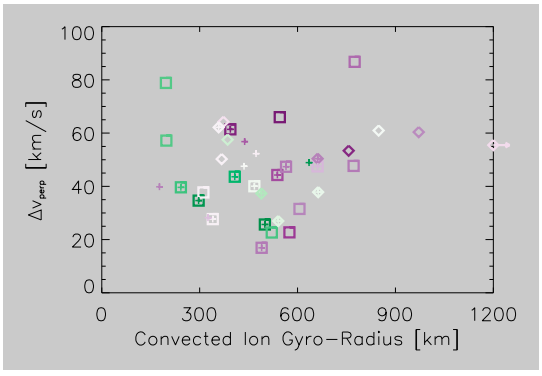

Figure 10. Peak transverse velocity deflection versus the convected ion gyroradius r_c in the upstream solar wind (same symbols and color code as Figures 6–9).

Small r_c also enables the reflected protons to reach speeds higher than the solar wind in a relatively confined spatial scale. This has the effect of reversing the direction of the momentum coupling force on the solar wind, allowing the momentum transfer to again reinforce the other fluid forces in a region downstream from the reflection point. We consider this effect qualitatively for the two events discussed in section 2 and shown in Figures 2 and 3. Figure 11 shows reflected proton trajectories for the two events, traced under the assumption of uniform

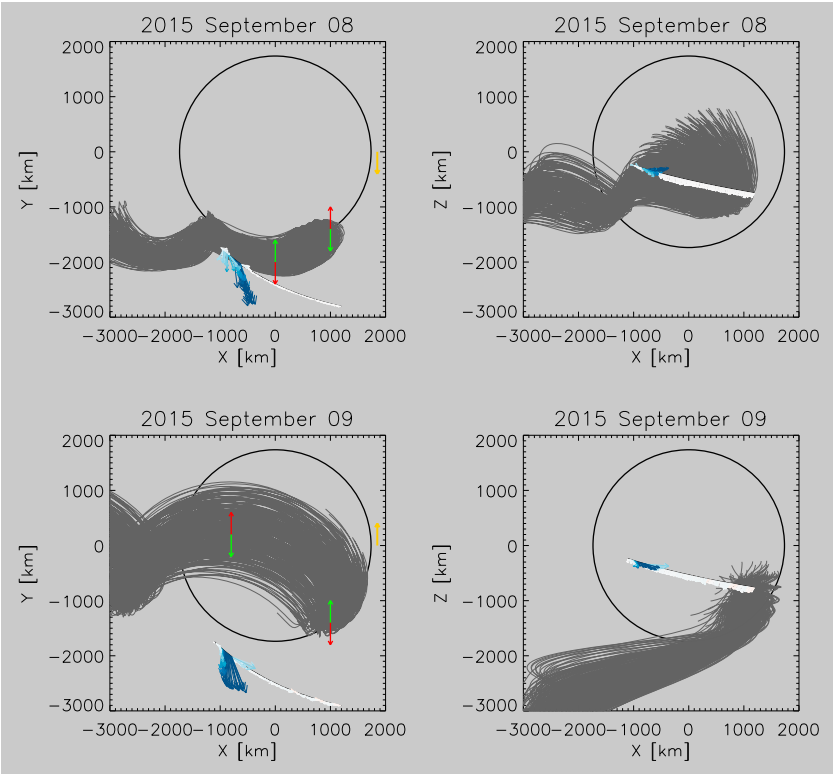

Figure 11. Reflected proton trajectories (gray lines) traced from the strong farside lunar magnetic anomalies under the assumption of uniform magnetic and electric fields equal to upstream values, along with observed velocity deflections (same color scale as Figures 5 and 6), for the events of Figure 2 (parallel case, top row) and Figure 3 (antiparallel case, bottom row). The orange arrows show direction of upstream motional electric field. The green and red arrows show the direction of the force on the reflected protons (green) and solar wind (red) at selected locations.

magnetic field and motional electric field (strictly valid only in the upstream region and when reflected densities remain small compared to the solar wind density, so these only provide a first-order approximation of the actual reflected proton trajectories).

We find that for the antiparallel case (Figure 11**,** bottom row, for the event of Figure 3, similar to the high-altitude event in *Halekas et al.* [2014] and the schematic illustration of Figure 1) reflected protons are quickly decelerated by the motional electric field, ultimately gyrating back and away from the limb (and in this case, southward). As a result, the solar wind experiences a momentum coupling force outward. The outward deflection observed by ARTEMIS occurs downstream, consistent with the expected location of a Mach surface beginning near the reflection point where the largest forces exist.

On the other hand, for the parallel case (Figure 11, top row, for the event of Figure 2), reflected protons accelerate outward along the motional electric field but follow smaller gyroorbits and therefore quickly reach energies higher than the solar wind energy (thanks to the smaller r_c). As a result, in an extended column upstream from the ARTEMIS observation, reflected protons have velocities greater than the solar wind, leading to an outward momentum coupling force on the solar wind core, again corresponding to the observations. In this case, a Mach surface may or may not form, and even if it exists it need not originate near the limb, but could start at any point along the column where the effects on the solar wind exceed a critical threshold.

6. Conclusions and Implications

Strong compressional disturbances, some of which may represent potentially the smallest collisionless shocks in the solar system, form near the Moon under a wide variety of solar wind conditions, including both steady and variable IMF conditions, and can extend to significant distances downstream from the Moon. We

show for the first time that events with velocity deflections parallel and antiparallel from the upstream motional electric field form in distinctly different solar wind conditions. We present a consistent framework that may explain many of the observed characteristics in terms of momentum transfer between the incoming solar wind and protons reflected from localized remanent crustal magnetic fields. Events with antiparallel deflections (analogous to the solitary shocks discussed by *Omidi and Sibeck* [2007]) occur more frequently, have larger magnetic amplifications, and occur predominantly in solar wind with lower magnetic fields, higher density, and higher β_p, M_A, and r_c. These characteristics favor momentum transfer between protons reflected from local magnetic fields and the incoming solar wind, forming a Mach surface extending downstream from near the reflection point. On the other hand, events with parallel deflections occur predominantly in solar wind with higher magnetic fields and lower β_p, M_A, and r_c. These characteristics favor momentum transfer from reflected protons accelerated to energies greater than the solar wind, which would take place downstream and laterally outward from the reflection location. If this explanation proves correct, it may help explain the apparent rarity of strong compressional events near the Moon, since only a specific combination of solar wind conditions, IMF geometry, and lunar phase will lead to the formation of a compression or shock at the location observed by ARTEMIS.

In conclusion, we point out that the compressional phenomena observed by ARTEMIS share many aspects with compressional phenomena that occur in the ion foreshock, with both arising as a result of proton reflection. In fact, for cases with variable IMF, we cannot at this time distinguish between lunar interactions and terrestrial foreshock interactions. However, the analogy may also hold for steady IMF conditions. In the case of the foreshock, proton reflection comes from the shock surface, while at the Moon it comes from localized lunar remanent magnetic fields (and most likely also from a shock surface in some cases). However, the ultimate result is an ion-ion interaction that can heat the plasma (both electrons and ions) and generate compressional disturbances, which in some cases can steepen to form small-scale shocks.

Acknowledgments
This research was supported by NASA grant NNX15AP89G and the Solar System Exploration Research Virtual Institute. We acknowledge NASA contract NAS5-02099 and V. Angelopoulos for the use of data from ARTEMIS, and specifically K.H. Glassmeier, U. Auster, and W. Baumjohann for the use of FGM data provided under the lead of the Technical University of Braunschweig and with financial support through the German Ministry for Economy and Technology and the German Center for Aviation and Space under contract 50 OC 0302. All data sets used in this study are publicly available at NASA's CDAWeb (http://cdaweb.nasa.gsfc.gov) and the ARTEMIS mission site (http://artemis.ssl.berkeley.edu). We thank a reviewer for excellent comments, which greatly strengthened the paper.

References

Angelopoulos, V. (2011), The ARTEMIS mission, *Space Sci. Rev.*, *165*, 3–25, doi:10.1007/s11214-010-9687-2.
Auster, H. U., et al. (2008), The THEMIS fluxgate magnetometer, *Space Sci. Rev.*, *141*, 235–264.
Bale, S. D., F. S. Mozer, and T. S. Horbury (2003), Density-transition scale at quasiperpendicular collisionless shocks, *Phys. Rev. Lett.*, *91*, doi:10.1103/PhysRevLett.91.265004.
Bale, S. D., et al. (2005), Quasi-perpendicular shock structure and processes, *Space Sci. Rev.*, *118*, 161–203.
Chapman, S. C., and M. W. Dunlop (1986), Ordering of momentum transfer along VvB in the AMPTE solar wind releases, *J. Geophys. Res.*, *91*, 8051–8055, doi:10.1029/JA091iA07p08051.
Colburn, D. S., J. D. Mihalov, and C. P. Sonett (1971), Magnetic observations of the lunar cavity, *J. Geophys. Res.*, *76*, 2940–2957, doi:10.1029/JA076i013p02940.
Coleman, P. J., Jr., G. Schubert, C. T. Russell, and L. R. Sharp (1972a), The particles and fields subsatellite magnetometer experiment, Apollo 15 Preliminary Science Report, *NASA Spec. Publ.*, *289*, 22-1–22-9.
Coleman, P. J., Jr., B. R. Lichtenstein, C. T. Russell, G. Schubert, and L. R. Sharp (1972b), The particles and fields subsatellite magnetometer experiment, Apollo 16 Preliminary Science Report, *NASA Spec. Publ.*, *315*, 23-1–23-13.
Deca, J., A. Divin, G. Lapenta, B. Lembège, S. Markidis, and M. Horányi (2014), Electromagnetic particle-in-cell simulations of the solar wind interaction with lunar magnetic anomalies, *Phys. Rev. Lett.*, doi:10.11103/PhysRevLett.112.151102.
Deca, J., A. Divin, B. Lembège, M. Horányi, S. Markidis, and G. Lapenta (2015), General mechanism and dynamics of the solar wind interaction with lunar magnetic anomalies from 3D PIC simulations, *J. Geophys. Res. Space Physics*, *120*, 6443–6463, doi:10.1002/2015JA021070.
Dyal, P., C. W. Parkin, and C. P. Sonett (1970), Apollo 12 magnetometer: Measurements of a steady magnetic field on the surface of the Moon, *Science*, *169*, 726.
Dyal, P., C. W. Parkin, and W. D. Daily (1974), Magnetism and the interior of the Moon, *Rev. Geophys. Space Phys.*, *12*, 568–591.
Fatemi, S., M. Holmström, Y. Futaana, C. Lue, M. R. Collier, S. Barabash, and G. Stenberg (2014), Effects of protons reflected by lunar crustal magnetic fields on the global lunar plasma environment, *J. Geophys. Res. Space Physics*, *119*, 6095–6105, doi:10.1002/2014JA019900.
Futaana, Y., S. Machida, Y. Saito, A. Matsuoka, and H. Hayakawa (2003), Moon-related nonthermal ions observed by Nozomi: Species, sources, and acceleration mechanisms, *J. Geophys. Res.*, *108*(A1), 1025, doi:10.1029/2002JA009366.
Futaana, Y., S. Barabash, M. Wieser, C. Lue, P. Wurz, A. Vorburger, A. Bhardwaj, and K. Asamura (2013), Remote energetic neutral atom imaging of electric potential over a lunar magnetic anomaly, *Geophys. Res. Lett.*, *40*, 262–266, doi:10.1002/grl.50135.
Giacalone, J., and L. L. Hood (2015), Hybrid simulation of the interaction of solar wind protons with a concentrated magnetic anomaly, *J. Geophys. Res. Space Physics*, *120*, 4081–4094, doi:10.1002/2014JA020938.
Halekas, J. S., D. A. Brain, D. L. Mitchell, R. P. Lin, and L. Harrison (2006), On the occurrence of magnetic enhancements caused by solar wind interaction with lunar crustal fields, *Geophys. Res. Lett.*, *33*, L01201, doi:10.1029/2006GL025931.
Halekas, J. S., D. A. Brain, R. P. Lin, and D. L. Mitchell (2008), Solar wind interaction with lunar crustal magnetic anomalies, *J. Adv. Space Res.*, *41*, 1319–1324, doi:10.1016/j.asr.2007.04.003.
Halekas, J. S., A. R. Poppe, J. P. McFadden, and K.-H. Glassmeier (2013), The effects of reflected protons on the plasma environment of the Moon for parallel interplanetary magnetic fields, *Geophys. Res. Lett.*, *40*, 4544–4548, doi:10.1002/grl.50892.
Halekas, J. S., A. R. Poppe, J. P. McFadden, V. Angelopoulos, K.-H. Glassmeier, and D. A. Brain (2014), Evidence for small-scale collisionless shocks at the Moon from ARTEMIS, *Geophys. Res. Lett.*, *41*, 7436–7443, doi:10.1002/2014GL061973.

Harnett, E. M., and R. M. Winglee (2000), Two-dimensional MHD simulations of the solar wind interaction with magnetic field anomalies on the surface of the Moon, *J. Geophys. Res.*, *105*, 24,997–25,007, doi:10.1029/2000JA000074.

Harnett, E. M., and R. Winglee (2003), 2.5-D fluid simulations of the solar wind interacting with multiple dipoles on the surface of the Moon, *J. Geophys. Res.*, *108*(A2), 1088, doi:10.1029/2002JA009617.

Hood, L. L., A. Zakharian, J. Halekas, D. L. Mitchell, R. P. Lin, M. H. Acuña, and A. B. Binder (2001), Initial mapping and interpretation of lunar crustal magnetic anomalies using Lunar Prospector magnetometer data, *J. Geophys. Res.*, *106*, 27,825–27,840, doi:10.1029/2000JE001366.

Jarvinen, R., M. Alho, E. Kallio, P. Wurz, S. Barabash, and Y. Futaana (2014), On vertical electric fields at lunar magnetic anomalies, *Geophys. Res. Lett.*, *41*, 2243–2249, doi:10.1002/2014GL059788.

Lin, R. P., D. L. Mitchell, D. W. Curtis, K. A. Anderson, C. W. Carlson, J. McFadden, M. H. Acuña, L. L. Hood, and A. Binder (1998), Lunar surface magnetic fields and their interaction with the solar wind: Results from Lunar Prospector, *Science*, *281*, 1480–1484.

Lue, C., Y. Futaana, S. Barabash, M. Wieser, M. Holmström, A. Bhardwaj, M. B. Dhanya, and P. Wurz (2011), Strong influence of lunar crustal fields on the solar wind flow, *Geophys. Res. Lett.*, *38*, L03202, doi:10.1029/2010GL046215.

McFadden, J. P., C. W. Carlson, D. Larson, M. Ludlam, R. Abiad, B. Elliott, P. Turin, M. Marckwordt, and V. Angelopoulos (2008), The THEMIS ESA plasma instrument and in-flight calibration, *Space Sci. Rev.*, *141*, 277–302.

Mitchell, D. L., J. S. Halekas, R. P. Lin, S. Frey, L. L. Hood, M. H. Acuna, and A. Binder (2008), Global mapping of lunar crustal magnetic fields by Lunar Prospector, *Icarus*, *194*, 401–409, doi:10.1016/j.icarus.2007.10.027.

Nakagawa, T., A. Nakayama, F. Takahashi, H. Tsunakawa, H. Shibuya, and H. Shimizu (2012), Large-amplitude monochromatic ULF waves detected by Kaguya at the Moon, *J. Geophys. Res.*, *117*, A04101, doi:10.1029/2011JA017249.

Ness, N. F., K. W. Behannon, H. E. Taylor, and Y. C. Whang (1968), Perturbations of the interplanetary magnetic field by the lunar wake, *J. Geophys. Res.*, *73*, 3421–3440, doi:10.1029/JA073i011p03421.

Nishino, M. N., M. Fujimoto, H. Tsunakawa, M. Matsushima, H. Shibuya, H. Shimizu, F. Takahashi, Y. Saito, and S. Yokota (2012), Control of lunar external magnetic enhancements by IMF polarity: A case study, *Planet. Space Sci.*, *73*(1), 161–167, doi:10.1016/j.pss.2012.09.011.

Omidi, N., and D. G. Sibeck (2007), Formation of hot flow anomalies and solitary shocks, *J. Geophys. Res.*, *112*, A01203, doi:10.1029/2006JA011663.

Omidi, N., X. Blanco-Cano, C. T. Russell, H. Karimabadi, M. Acuña (2002), Hybrid simulations of solar wind interaction with magnetized asteroids: General characteristics, *J. Geophys. Res.*, *107*(A12), 1487, doi:10.1029/2002JA009441.

Russell, C. T., and B. R. Lichtenstein (1975), On the source of lunar limb compressions, *J. Geophys. Res.*, *80*, 4700–4711, doi:10.1029/JA080i034p04700.

Saito, Y., et al. (2010), Inflight performance and initial results of Plasma energy Angle and Composition Experiment (PACE) on SELENE (Kaguya), *Space Sci. Rev.*, *154*, 265.

Saito, Y., M. N. Nishino, M. Fujimoto, T. Yamamoto, S. Yokota, H. Tsunakawa, H. Shibuya, M. Matsushima, H. Shimizu, and F. Takahashi (2012), Simultaneous observation of the electron acceleration and ion deceleration over lunar magnetic anomalies, *Earth Planets Space*, *64*, 83–92.

Sauer, K., A. Bogdanov, and K. Baumgärtel (1994), Evidence of an ion composition boundary (protonopause) in bi-ion fluid simulations of solar wind mass loading, *Geophys. Res. Lett.*, *21*, 2255–2258, doi:10.1029/94GL01691.

Schubert, G., and B. R. Lichtenstein (1974), Observations of Moon -plasma interactions by orbital and surface experiments, *Rev. Geophys.*, *12*, 592–626, doi:10.1029/RG012i004p00592.

Schwartz, S. J. (1995), Hot flow anomalies near the Earth's bow shock, *Adv. Space Res.*, *15*, 107–116.

Siscoe, G. L., E. F. Lyon, J. H. Binsach, and H. S. Bridge (1969), Experimental evidence for a detached lunar compression wave, *J. Geophys. Res.*, *74*, 59–69, doi:10.1029/JA074i001p00059.

Sonett, C. P., and J. D. Mihalov (1972), Lunar fossil magnetism and perturbations of the solar wind, *J. Geophys. Res.*, *77*, 588–603, doi:10.1029/JA077i004p00588.

Thomas, V. A., D. Winske, M. F. Thomsen, and T. G. Onsager (1991), Hybrid simulation of the formation of a hot flow anomaly, *J. Geophys. Res.*, *961*, 11,625–11,632, doi:10.1029/91JA01092.

Tsunakawa, H., F. Takahashi, H. Shimizu, H. Shibuya, and M. Matsushima (2015), Surface vector mapping of magnetic anomalies over the Moon using Kaguya and Lunar Prospector observations, *J. Geophys. Res. Space Physics*, *120*, 1160–1185, doi:10.1002/2014JE004785.

Whang, Y. C., and N. F. Ness (1970), Observations and interpretation of the lunar Mach cone, *J. Geophys. Res.*, *75*, 6002–6010, doi:10.1029/JA075i031p06002.

Whang, Y. C., and N. F. Ness (1972), Magnetic-field anomalies in the lunar wake, *J. Geophys. Res.*, *77*, 1109–1115, doi:10.1029/JA077i007p01109.

Wieser, M., S. Barabash, Y. Futaana, M. Holmström, A. Bhardwaj, R. Sridharan, M. B. Dhanya, A. Schaufelberger, P. Wurz, and K. Asamura (2010), First observation of a mini-magnetosphere above a lunar magnetic anomaly using energetic neutral atoms, *Geophys. Res. Lett.*, *37*, L05103, doi:10.1029/2009GL041721.

Zhang, H., K. K. Khurana, M. G. Kivelson, V. Angelopoulos, W. X. Wan, L. B. Liu, Q.-G. Zong, Z. Y. Pu, Q. Q. Shi, and W. L. Liu (2014), Three-dimensional lunar wake reconstructed from ARTEMIS data, *J. Geophys. Res. Space Physics*, *119*, 5220–5243, doi:10.1002/2014JA020111.